 doi:10.20944/preprints201810.0353.v1

Experimental and Numerical Investigations into the failure mechanisms of TRIP700 steel sheets

N. Habibi[1], V. Sundararaghavan[2], U. Prahl[3], A. Ramazani[2*]

[1]*Department of Ferrous Metallurgy, RWTH Aachen University, Germany*

[2]*Department of Aerospace Engineering, University of Michigan-Ann Arbor, USA*

[3]*Institute of Metal Forming, Freiberg University of Mining and Technology, Germany*

Abstract

The formability and failure behavior of TRIP steel blanks were investigated through various stress states. The forming limit diagram (FLD) at fracture is constructed both experimentally and numerically. Numerical studies are performed to evaluate the applicability of different damage criteria in predicting the FLD as well as complex cross-die deep drawing process. The fracture surface and numerical results revealed that the material failed in a different mode for different strain path. Therefore, Tresca model which is based on shear stress accurately predicted the conditions where shear had the profound effect on the damage initiation, whereas Situ localized necking criterion was able to calculate the conditions which localization was dominant.

Keywords: TRIP steel sheet, Cross-die test, Forming limit diagram, Finite element analysis, Failure mechanisms

[*] Corresponding author: Tel: +1 734 353 3569; fax: +49 241 80 92253.
E-mail address: ramazani@umich.edu (A. Ramazani)

Preprints (www.preprints.org) | NOT PEER-REVIEWED | Posted: 16 October 2018 doi:10.20944/preprints201810.0353.v1

Nomenclature	
A, B, C	strain hardening parameters, various dimensions
E	experimental results, in this study the results of equivalent strains
F, G, H	Parameters of Hill 1948 criterion
r_ϕ	anisotropic coefficients at $\phi°$ from the rolling direction, dimensionless
$\bar{r}$	normal anisotropy coefficient, dimensionless, $\bar{r} = \frac{r_0+2r_{45}+r_{90}}{4}$
Δr	planar anisotropy coefficient, dimensionless, $\Delta r = \frac{r_0-2r_{45}+r_{90}}{2}$
R_{ij}	Anisotropic yield stress ratio, dimensionless, $R_{ij} = \begin{cases} \frac{\sigma_{ij}}{\sigma_0}, i = j \\ \frac{\sqrt{3}\sigma_{ij}}{\sigma_0}, i \neq j \end{cases}$
P	predicted results, in this study the results of equivalent strains
$\bar{\varepsilon}$	effective or equivalent plastic strain, dimensionless
ε_i	logarithmic strain components, dimensionless
ρ	strain path, dimensionless, $\rho = \frac{d\varepsilon_2}{d\varepsilon_1}$
$\bar{\sigma}$	effective or equivalent stress, MPa
σ_i	Cauchy stress components, MPa
σ_Y	Yield stress, MPa
τ_{max}	maximum shear stress, MPa

 doi:10.20944/preprints201810.0353.v1

1. Introduction

Transformation-induced-plasticity (TRIP) steels sheets are widely used in automotive structures due to their outstanding mechanical properties, like the forming potential and high energy absorption [1-5]. However, the application of high strength steels requires thorough knowledge of their formability behavior. Forming limit diagram at necking (FLD) is an indispensable tool for evaluating sheet metal formability at the industrial level. This diagram represents the maximum values of major strain-minor strain pairs at the onset of localized necking in a sheet subjected to different proportional linear strain paths. In this way, a boundary is established between strain states that facilitate sheet forming and those that lead the sheets into failure [6,7].

However, the experimental determination of sheet formability is accompanied by many complications and is a time-consuming procedure. Therefore, theoretical prediction methods have been taken into consideration for calculating and constructing the forming limit diagram for different materials. In this regard, several models have been proposed to calculate damage initiation. The well-known models are considered, Marciniak-Kuczynski (M-K) [8], and Gurson-Tvergaard-Needleman (GTN) [9], which are extensively used for different materials and processes [10-13], due to the fact that they can relatively simply and easily be employed and the results are mostly accurate. Panich et al. [12] calculated both strain and stress based forming limit diagrams using M-K model for TRIP780. The results stated that stress based FLD was able to predict failure in the material. However, as the stresses could not be measured directly, it depended on used strain hardening law and yielding model. Bhargava et al. [14] applied different failure criteria to construct FLD of a TRIP steel. The results implied that its FLD was better predicted by the model which detected the deviation of major strain than punch force, thickness, and equivalent plastic strain. Paul [15] predicted FLD for various auto grade steel sheets among TRIP780 by developing a nonlinear regression equation. The results matched well with the experimental results, however for calibrating the model several experimental tests were performed.

The objective of the present work is to evaluate the ability of different damage criteria to predict the forming limits of TRIP700 steel sheet. The damage models selected based on specific characteristics, including simplicity, ease of use, and least dependence on the

Preprints (www.preprints.org) | NOT PEER-REVIEWED | Posted: 16 October 2018 doi:10.20944/preprints201810.0353.v1

experimental calibration. The capability of the models in damage prediction for the studied steel was assessed through Nakazima punch stretching and cross-die deep drawing tests in order to induce linear and non-linear strain paths, respectively. Cross-die deep drawing test is a new experimental technique, which was originally designed by the automotive industry as a press-shop formability test technique [13,16,17]. Since this method is able to trigger a wide variety of stress states, i.e. from uniaxial tension to plane-strain, and biaxial tension, it is a good candidate to evaluate the formability of sheets.

2. Experimental procedure

2.1. Material

The formability of a TRIP700 steel sheet with a thickness of 1.2 mm was investigated. The chemical composition is represented in Table 1, and the initial microstructure is shown in Fig.1. The mechanical properties were evaluated through different directions by using tensile tests according to DIN EN 10002 standard and hydraulic bulge tests [18]. The data is illustrated in Fig. 2 and Table 2.

2.2. Nakazima punch stretching test

The experimental forming limit diagram was calculated using Nakazima testing method. In this regard, different specimens with various geometries were first prepared, and then square grid patterns were etched electrochemically on their surface for strain analysis. The specimens were formed up to fracture and the limiting strains at necking and fracture areas were evaluated. Schematic geometries of specimens and the machine used for the forming process are illustrated In Fig. 3.

2.3. Cross-die test

The cross-die deep drawing is able to cover a wide range of stress states. The experimental setup and the final product configuration, are shown in Fig. 4. The side dimensions of initial square blanks were about 270 mm. Special oil with a friction coefficient of 0.05 was used to lubricate the steel surfaces. The punching speed was set at 35 mm/s and the blank holder force was set at 667 kN. The strain distribution of the products was measured with PHAST™ photogrammetric strain measuring equipment.

3. Numerical procedure

3.1. Failure criteria

In order to design a successful forming process, prediction of fracture probability during deformation is vital. In this respect, various theories have been introduced to detect the

Preprints (www.preprints.org) | NOT PEER-REVIEWED | Posted: 16 October 2018 doi:10.20944/preprints201810.0353.v1

onset of sheet metals' failure which mostly based on deriving strains of necking region which lead to fracture. In the present study, three different failure criteria have been applied to calculate the forming limit strains for the different strain paths, as listed in Table 3, and illustrated in Fig.5.

1- As the experimental observations in sheet metals [19] show that the fracture plane inclined towards a direction which contains maximum shear stress, a shear failure model has been used. Tresca criterion predicts the onset of necking, based on a macroscopic function which describes damage accumulation [20], Eq. 1.

2- Situ et al. [21,22] proposed a localized necking model according to a physical viewpoint. In this criterion, when a critical element exhibits an inflection in its major strain rate history, the localized necking initiates. This inflection corresponds to a maximum in the major strain acceleration, Eq. 2.

3-In the other physical criterion which is suggested by Martínez-Donaire et al. [23], the influence of localized necking zone on the adjacent elements is considered. According to this theory, the strain rate of the adjacent elements to the necking zone is gradually reduced as the strain rate evolution ceases, Eq. 3. In other words, these elements reach a constant level of strain or even undergo some elastic unloading before the fracture initiates, i.e. the deformation is only accompanied by elements in the necking zone.

3.2. Numerical simulation

3.2.1. Plasticity

The theoretical basis of the failure models has already been described. The assumptions used in these analyses are as follows:

1. Plane stress conditions, i.e. $\sigma_3 = 0$.
2. Plastic incompressibility during deformation, i.e. $d\varepsilon_1 + d\varepsilon_2 + d\varepsilon_3 = 0$.
3. Hill's quadratic yield criterion [24] for planar isotropic materials,

$$\bar{\sigma}^2 = F\sigma_2{}^2 + G\sigma_1{}^2 + H(\sigma_1 - \sigma_2)^2 \quad (4)$$

where,

$$F = \frac{r_0}{(1+r_0)r_{90}}, G = \frac{1}{(1+r_0)}, H = \frac{r_0}{(1+r_0)} \quad (5)$$

4. Associated flow rules,

$$d\varepsilon_i = d\lambda\left(\frac{\partial\bar{\sigma}}{\partial\sigma_i}\right) \quad (6)$$

5. An equivalent strain function,

$$\bar{\sigma}d\bar{\varepsilon} = \sigma_1 d\varepsilon_1 + \sigma_2 d\varepsilon_2 \quad (7)$$

Preprints (www.preprints.org) | NOT PEER-REVIEWED | Posted: 16 October 2018 doi:10.20944/preprints201810.0353.v1

6. An assumption of a linear proportional strain path, i.e. $\rho = \frac{d\varepsilon_2}{d\varepsilon_1} = \text{constant}$.

7. Voce hardening law:

$$\bar{\sigma} = A + (B - A) * \exp(-C\bar{\varepsilon}_p) \quad (8)$$

To apply any failure criteria, it is crucial to interpreting the complete stress–strain history of material during the deformation process. For this purpose, the Cauchy stress components (σ_{ij}) and the logarithmic plastic strain components (ε_{ij}), which are difficult to acquire directly from the experimental tests, were derived from the parallel numerical simulations (explained in the following section) at location of the failure. Furthermore, the other parameters were calculated by using above equations. It is worth mentioning that Tresca model was calibrated through both experimental and simulation results of the hemispherical punch tests from the specimens with 45 mm width, i.e. $(\tau_{max})_{critical}$ = 539 MPa.

3.2.2. Finite element method

The 3D finite element method simulations using commercial finite element code Abaqus/Explicit 6.14 have been performed to analyze the Nakazima punch stretching and cross-die tests. The die, punch, and blank holder were defined as analytical rigid parts, and the sheet was assigned as a deformable homogenous shell (all dimensions were according to the experimental set-ups). The mechanical properties were extracted from the uniaxial tensile test. Hill 1948 criterion was adapted to simulate the yielding and the frictional conditions were considered by Coulomb friction model. The simulation and material data are given in Table 4. A four-node quadrilateral shell element (S4R) with the size of 0.4×0.4 mm^2 was employed. The mass scaling factor has been defined, therefore it was made certain that the ratio of kinetic energy to internal energy would not become too large. To reduce the computational time, the mass scaling factor was assumed to be equal to 1000. After clamping, the holder was fixed and the punch was moved towards the sheet. The optimal clamping force was chosen such that the blank neither drew-in nor tore near the draw bead during forming. The examined elements were chosen based on the experimental fracture site and the assumption of each criteria.

4. Results and discussion

Three different damage models have been considered to predict the formability of TRIP700 steel sheets through various stress states. In order to present the results properly, this section

Preprints (www.preprints.org) | NOT PEER-REVIEWED | Posted: 16 October 2018 doi:10.20944/preprints201810.0353.v1

is divided into two parts which are based on the testing techniques that are utilized. In each part, the experimental and numerical results are discussed.

4.1. Nakazima punch stretching tests

The experiments were carried out for different geometries to induce various strain paths and the FLD was calculated, Fig. 6. The simulation results, which were performed according to the experimental tests, show each specimen experienced a specific, almost linear strain path before fracture and the designed specimens were able to cover a wide range of strain paths, Fig. 6, from uniaxial tension to equi-biaxial tension. The calculated FLD illustrates relatively low forming limits in comparison to other high strength steels [26,27]. The accuracy of the simulations was evaluated by the deformation history and failure location for all specimens as well, Fig. 7.

Concerning the fracture surfaces analysis, we refer to literature results from stretched specimens in the different deformation conditions made by Quade [28] as shown in Fig. 8. In the low magnifications, the surfaces seem to be smooth as brittle fracture characteristic. However, by increasing the magnification very fine dimples reveal the ductile dominant feature of fracture for this material. Although they are different in number, size, and depth for each strain path. As observed in Fig. 8, fracture surface of all the specimens show a bimodal distribution of large stringers and fine equi-axed dimples, as reported for other high strength steels [29]. It is worth mentioning the uniaxial tension mode would force the voids to incline towards the loading direction and restrict their growth. It is caused due to the low stress-triaxiality of this mode which approaches the pure shearing condition [30-32]. The increase in stress-triaxiality leads more void growth and coalescence, which line up more parallel to the loading direction. The existence of fine voids implies the occurrence of shear coalescence, which suppresses large expansion in the voids' volume [33]. The large stringers of voids indicate the primary voids, which underwent significant growth along the fracture surface.

The forming limits were calculated using the damage models described before. In addition, the capacity of each model in forming limits prediction was assessed, Fig. 9 (b), by statistical analysis of the relative error, calculated by the following equation:

$$\text{Relative error} = \left(\frac{P-E}{E}\right) \times 100\%$$

The results show that all the models are able to predict the strain paths near plane strain mode relatively in good agreement to the experiment, i.e. for specimens with 30, 45, and 60 mm

Preprints (www.preprints.org) | NOT PEER-REVIEWED | Posted: 16 October 2018 doi:10.20944/preprints201810.0353.v1

width. Nevertheless, the uniaxial tension mode, 15-mm width specimen, was calculated well by Tresca model. It is related to the fact that this condition is near pure shear mode and the effect of shear stress is dominant, as illustrated in Fig. 8 (b). Although, the equi-biaxial condition is better predicted by Situ model than by Tresca. It implies that the material underwent more localized necking in this stress state, as approved in Fig. 6 where the strain path is gradually changing to plane strain mode, and in Fig. 8 more and deeper dimples can be observed throughout the fracture surface. Although it should be noted that the creation of localized necking may not necessarily induce plane strain state immediately. Even after necking, the minor strain keeps varying to some extent as the neck grows [34]. The results of Martínez-Donaire criterion always inclined between the other two models, which imply that the model defines damage not based on the effect of shear stress. Although, it should be always less than Situ model, since the data is gathered from an adjacent element in the instability region which seems to be more sensitive to necking. Note that the region of instability, or necking region, included all points that increased monotonically their level of strain until fracture occurred.

4.2. Cross-die deep drawing tests

The cross-die deep drawing tests were carried out for two different height, 39.5 and 48.6 mm which led into safe and critical products, respectively. The strain distribution measurements for the products by PHAST^{TM} equipment, Fig. 10. In both products, the strain distributions are far above the forming limit curve, which was calculated by Nakazima punch-stretching tests, (up to 12%). The minor and major strains of the 48.6-mm-height product were illustrated in Fig. 11. The strain path analysis of cross-die tests reveals the complex forming process, Fig. 11 (c).

Fig. 12-14 show the simulation results of the cross-die test. The fracture location and the force-displacement response were predicted precisely. The strain distribution and product height at the onset of damage were obtained through different damage models. In addition, the experimental FLD was considered as one of the damage models. It is worth mentioning that the shape and concavity of the FLD has strong effect on the prediction of damage location. Therefore, these results of cross-die test are different from the ones for DP600 [35]. The capability of the models in damage prediction was illustrated in Fig. 15. Although predicted FLDs at plane strain condition were close to the experimental data, the precision was reduced for other conditions. It is worth mentioning that some negligible errors might occur in both the experimental and numerical approaches. For instance, in FE simulations the parameters which are supposed to have minor effects on the final results are eliminated, such

 doi:10.20944/preprints201810.0353.v1

as temperature, adiabatic heating, and strain rate. In addition, in experiment stopping the process at the exact moment of the fracture onset is very difficult.

However, the location of failure for experiments and simulations are in good agreement. Note that the bending effects result in some differences between integration points on the top or bottom surfaces. The strain states of the integration points on the inside (−) and outside (+) surfaces at the fracture moment are plotted in Fig. 13 (a) and (b), respectively. These point out that the failure triggered outside of the cross-die product, based on experimental FLD.

5. Conclusion

The formability of sheet metals is mostly limited by the occurrence of localized necking, i.e. non-uniform strains within a small region in the plane of the sheet. Therefore, estimation of materials' formability plays a principal role in the design of sheet forming processes. In this regard, applying simple accurate models are highly beneficial. In this study, three simple damage models were employed on the data of Nakazima punch stretching and cross-die deep drawing tests. The results show that the material failed in different modes for different strain path. When the shear failure was dominant, like uniaxial tension, the Tresca model was able to calculate the damage initiation. Whereas, for the conditions which the localized necking caused damage initiation, like equi-biaxial tension, the Situ model predicted precisely.

Acknowledgements

This research was carried out under Project Number MC2.07293 in the framework of the Research Program of the Materials innovation institute M2i (www.m2i.nl).

References

1. Tamura, I. Deformation-induced martensitic transformation and transformation-induced plasticity in steels. *Metal Science* **1982**, *16*, 245-253.
2. Fischer, F.-D.; Reisner, G.; Werner, E.; Tanaka, K.; Cailletaud, G.; Antretter, T. A new view on transformation induced plasticity (TRIP). *International Journal of Plasticity* **2000**, *16*, 723-748.
3. Ramazani, A.; Bruehl, S.; Gerber, T.; Bleck, W.; Prahl, U. Quantification of bake hardening effect in DP600 and TRIP700 steels. *Materials & Design* **2014**, *57*, 479-486.
4. Luo, H.; Dong, H. New ultrahigh-strength Mn-alloyed TRIP steels with improved formability manufactured by intercritical annealing. *Materials Science and Engineering: A* **2015**, *626*, 207-212.
5. Ramazani, A.; Quade, H.; Abbasi, M.; Prahl, U. The effect of martensite banding on the mechanical properties and formability of TRIP steels. *Materials Science and Engineering: A* **2016**, *651*, 160-164.
6. Goodwin, G.M. Application of strain analysis to sheet metal forming problems in the press shop. *SAE Transactions* **1968**, 380-387.

7. Keeler, S.P. Circular grid system—a valuable aid for evaluating sheet metal formability. *SAE Transactions* **1968**, 371-379.
8. Marciniak, Z.; Kuczyński, K.; Pokora, T. Influence of the plastic properties of a material on the forming limit diagram for sheet metal in tension. *International Journal of Mechanical Sciences* **1973**, *15*, 789-800.
9. Tvergaard, V.; Needleman, A. Analysis of the cup-cone fracture in a round tensile bar. *Acta metallurgica* **1984**, *32*, 157-169.
10. Choi, K.S.; Liu, W.N.; Sun, X.; Khaleel, M.A. Microstructure-based constitutive modeling of TRIP steel: Prediction of ductility and failure modes under different loading conditions. *Acta Materialia* **2009**, *57*, 2592-2604.
11. Uthaisangsuk, V.; Prahl, U.; Bleck, W. Modelling of damage and failure in multiphase high strength DP and TRIP steels. *Engineering Fracture Mechanics* **2011**, *78*, 469-486.
12. Panich, S.; Barlat, F.; Uthaisangsuk, V.; Suranuntchai, S.; Jirathearanat, S. Experimental and theoretical formability analysis using strain and stress based forming limit diagram for advanced high strength steels. *Materials & Design* **2013**, *51*, 756-766.
13. Ramazani, A.; Abbasi, M.; Prahl, U.; Bleck, W. Failure analysis of DP600 steel during the cross-die test. *Computational Materials Science* **2012**, *64*, 101-105.
14. Bhargava, M.; Tewari, A.; Mishra, S.K. Forming limit diagram of Advanced High Strength Steels (AHSS) based on strain-path diagram. *Materials & Design* **2015**, *85*, 149-155.
15. Paul, S.K. Prediction of complete forming limit diagram from tensile properties of various steel sheets by a nonlinear regression based approach. *Journal of Manufacturing Processes* **2016**, *23*, 192-200.
16. Lingbeek, R.; Meinders, T.; Rietman, A. Tool and blank interaction in the cross-die forming process. *International Journal of Material Forming* **2008**, *1*, 161-164.
17. Niazi, M.S.; Wisselink, H.; Meinders, T.; Huétink, J. Failure predictions for DP steel cross-die test using anisotropic damage. *International journal of damage mechanics* **2012**, *21*, 713-754.
18. Bleck, W.; Blumbach, M. Laser‐Aided Flow Curve Determination in Hydraulic Bulging. *steel research international* **2005**, *76*, 125-130.
19. Bressan, J.; Williams, J. The use of a shear instability criterion to predict local necking in sheet metal deformation. *International Journal of Mechanical Sciences* **1983**, *25*, 155-168.
20. Rice, J.R. The localization of plastic deformation. **1976**.
21. Situ, Q.; Jain, M.; Metzger, D. Determination of forming limit diagrams of sheet materials with a hybrid experimental–numerical approach. *International Journal of Mechanical Sciences* **2011**, *53*, 707-719.
22. Situ, Q.; Jain, M.K.; Bruhis, M. A suitable criterion for precise determination of incipient necking in sheet materials. In Proceedings of Materials science forum; pp. 111-116.
23. Martínez-Donaire, A.; García-Lomas, F.; Vallellano, C. New approaches to detect the onset of localised necking in sheets under through-thickness strain gradients. *Materials & Design* **2014**, *57*, 135-145.
24. Hill, R. A theory of the yielding and plastic flow of anisotropic metals. In Proceedings of Proceedings of the Royal Society of London A: Mathematical, Physical and Engineering Sciences; pp. 281-297.
25. Ghosh, A.K. A method for determining the coefficient of friction in punch stretching of sheet metals. *International Journal of Mechanical Sciences* **1977**, *19*, 457-470.

26. Bleck, W.; Deng, Z.; Papamantellos, K.; Gusek, C.O. A comparative study of the forming-limit diagram models for sheet steels. *Journal of Materials Processing Technology* **1998**, *83*, 223-230.
27. Anderson, D. Application and repairability of advanced high-strength steels. American Iron and Steel Institute. 2008.
28. Quade, H. Mechanical Properties, Damage Behaviour and Retained Austenite Stability in Low-Alloyed Trip Steels - Experimental & Numerical Analyses (Berichte aus dem Institut fur Eisenhuttenkunde). *Shaker Verlag GmbH, Germany* **2014**, 114-116.
29. Savic, V.; Hector Jr, L.; Fekete, J. Digital image correlation study of plastic deformation and fracture in fully martensitic steels. *Experimental Mechanics* **2010**, *50*, 99-110.
30. Kang, J.; Wilkinson, D.S.; Bruhis, M.; Jain, M.; Wu, P.D.; Embury, J.D.; Mishra, R.K.; Sachdev, A.K. Shear localization and damage in AA5754 aluminum alloy sheets. *Journal of Materials Engineering and Performance* **2008**, *17*, 395-401.
31. Habibi, N.; Zarei-Hanzaki, A.; Abedi, H.-R. An investigation into the fracture mechanisms of twinning-induced-plasticity steel sheets under various strain paths. *Journal of Materials Processing Technology* **2015**, *224*, 102-116.
32. Situ, Q.; Jain, M.K.; Bruhis, M. Further experimental verification of a proposed localized necking criterion. In Proceedings of AIP Conference Proceedings; pp. 907-912.
33. Teirlinck, D.; Zok, F.; Embury, J.; Ashby, M. Fracture mechanism maps in stress space. *Acta Metallurgica* **1988**, *36*, 1213-1228.
34. Situ, Q.; Bruhis, M.; Jain, M. Obtaining Formability Characteristics Of Automotive Materials Using On‐line Strain Imaging System. In Proceedings of AIP Conference Proceedings; pp. 131-135.
35. Habibi, N.; Ramazani, A.; Sundararaghavan, V.; Prahl, U. Failure predictions of DP600 steel sheets using various uncoupled fracture criteria. *Engineering Fracture Mechanics* **2018**, *190*, 367-381.

Preprints (www.preprints.org) | NOT PEER-REVIEWED | Posted: 16 October 2018 doi:10.20944/preprints201810.0353.v1

Tables

Table 1. Chemical composition of the investigated TRIP700 steel (wt. %).

C	Mn	Si	Al	N	P	S	V	Ti	Fe
0.187	1.620	0.350	0.917	>0.001	0.087	0.003	0.003	0.009	Bal.

Table 2. Lankford coefficients (r-values).

r_0	r_{45}	r_{90}	$\bar{r}$	Δr
0.793	0.909	1.035	0.912	0.005

Table 3. The failure criteria were used in the study.

Criterion	Equation
Tresca [20]	$\tau_{max} \geq (\tau_{max})^*_{critical}$ ..... (1)
Q. Situ et al. [21]	$\left(d^2\varepsilon_1/dt^2 = \max\right)_{\text{at the failure zone}}$ ..... (2)
A.J. Martínez-Donaire et al. [22]	$\left(d\varepsilon/dt = \max\right)_{\text{at the adjacent of failure zone}}$ ..... (3)

*$(\tau_{max})_{critical}$ is a material constant which calibrated by the experimental results of 25-mm width specimen of hemispherical-punch test along with numerical simulation, in the present study.

Preprints (www.preprints.org) | NOT PEER-REVIEWED | Posted: 16 October 2018 doi:10.20944/preprints201810.0353.v1

Table4. The utilized data for numerical simulation.

Simulation data					
Friction coefficient					
blank-punch interface				0.05	
blank-matrix interface				0.10	
blank-holder interface				0.10	
Material data					
Density (kg m^{-3})				7800	
Young's modulus (GPa)				210	
Poisson ratio				0.3	
Hardening law of the base material					
A		B		C	
1099.98		520.90		6.27	
R_{11}	R_{22}	R_{33}	R_{12}	R_{23}	R_{13}
1	1.0724	1.0076	1.0396	1	1

* $\mathbf{R_{11} = R_{13} = R_{23} = 1, R_{22} = \sqrt{\frac{r_{90}(r_0+1)}{r_0(r_{90}+1)}}, R_{33} = \sqrt{\frac{r_{90}(r_0+1)}{(r_0+r_{90})}}, R_{12} = \sqrt{\frac{3r_{90}(r_0+1)}{(2r_{45}+1)(r_0+r_{90})}}}$

 doi:10.20944/preprints201810.0353.v1

Figures

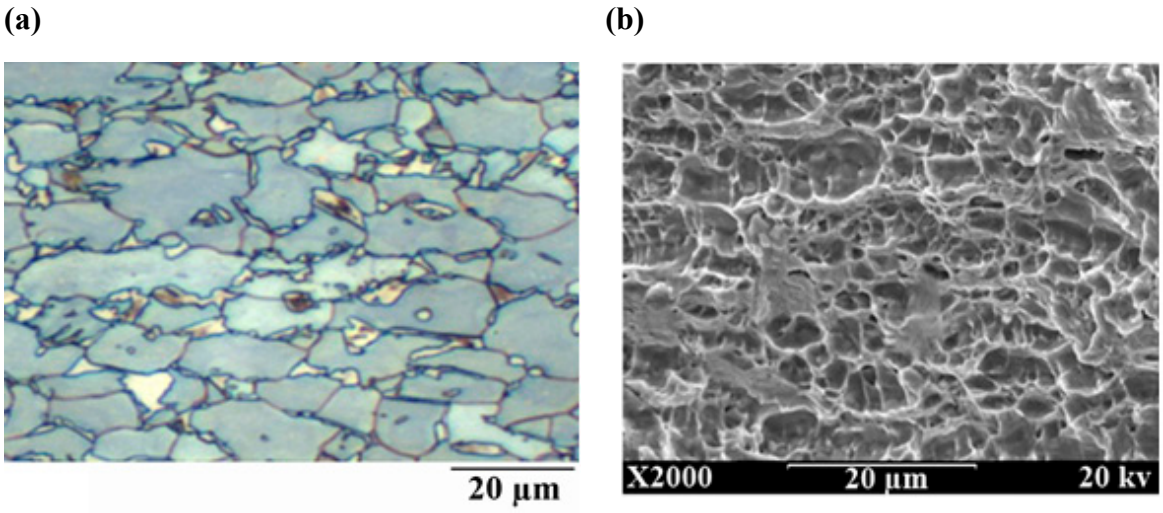

Fig. 1. (a) As-received microstructure, and (b) fracture surface of the studied TRIP700 steel.

Preprints (www.preprints.org) | NOT PEER-REVIEWED | Posted: 16 October 2018 doi:10.20944/preprints201810.0353.v1

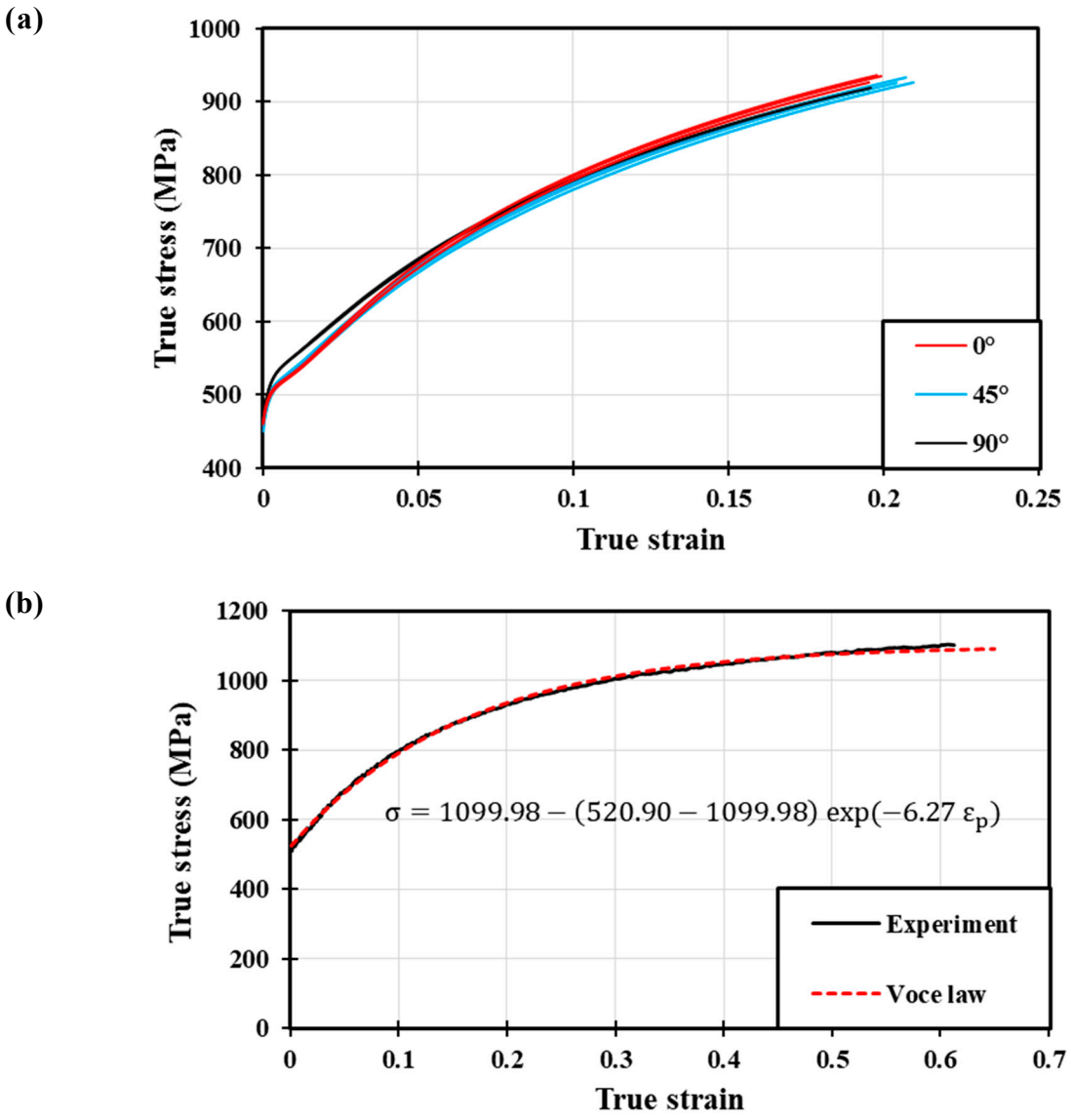

Fig. 2. The flow curve of TRIP700 steel; through (a) uniaxial tension tests at different directions from the rolling direction, and (b) bulge test with fitted strain hardening curve.

Preprints (www.preprints.org) | NOT PEER-REVIEWED | Posted: 16 October 2018 doi:10.20944/preprints201810.0353.v1

(a)

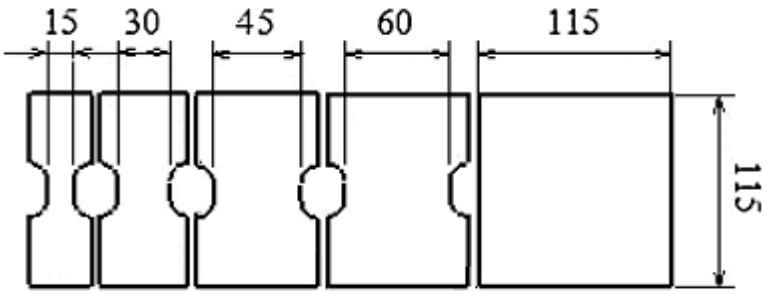

(b)

Fig. 3. Nakazima stretch-forming test; (a) geometries of the specimens (all dimensions in mm), and (b) the test set-up.

Preprints (www.preprints.org) | NOT PEER-REVIEWED | Posted: 16 October 2018 doi:10.20944/preprints201810.0353.v1

(a) **(b)**

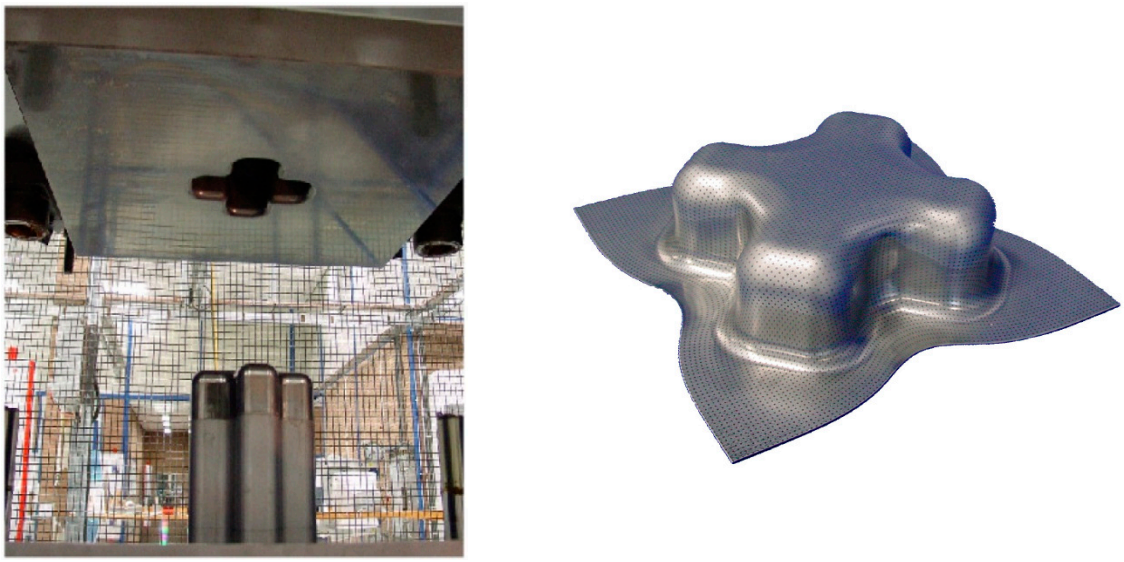

Fig. 4. Cross-die test; (a) the set-up, and (b) the final production.

Preprints (www.preprints.org) | NOT PEER-REVIEWED | Posted: 16 October 2018 doi:10.20944/preprints201810.0353.v1

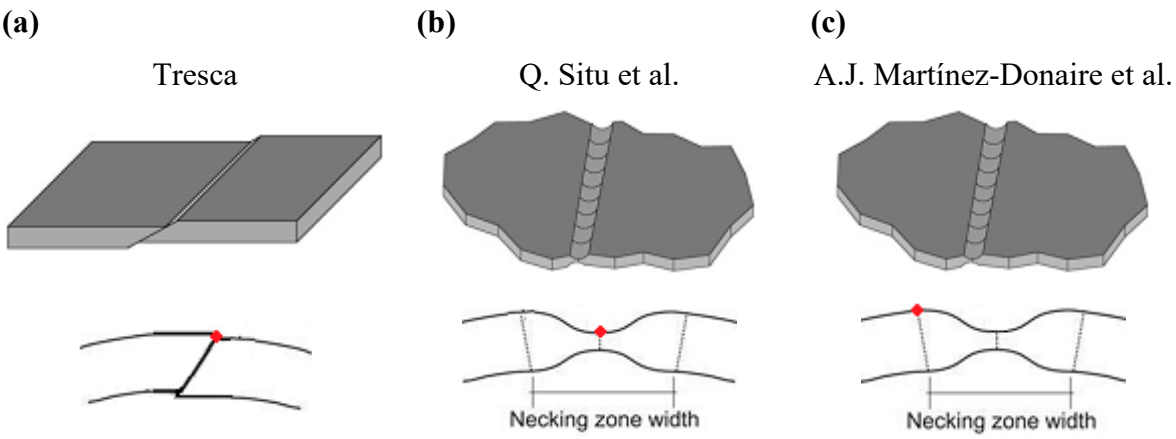

Fig. 5. Illustration of the investigated point in each failure criterion.

Preprints (www.preprints.org) | NOT PEER-REVIEWED | Posted: 16 October 2018 doi:10.20944/preprints201810.0353.v1

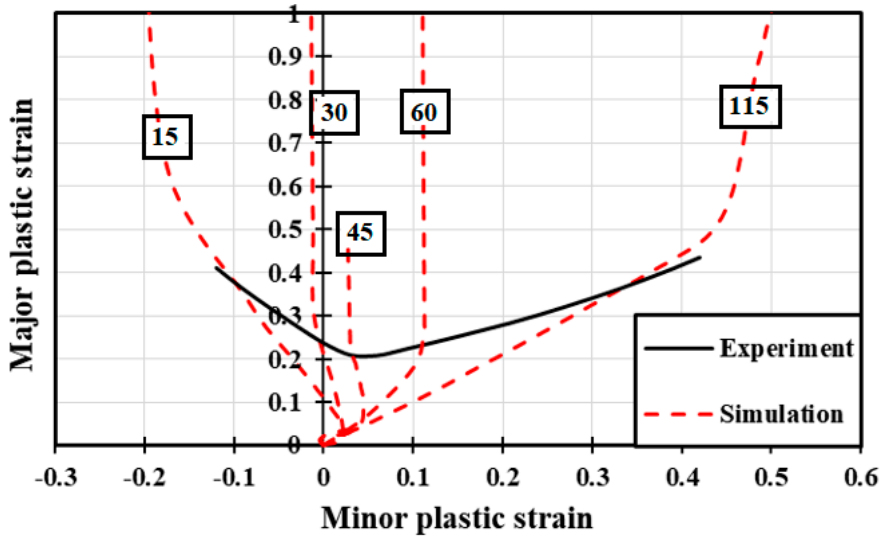

Fig. 6. The calculated strain path of each specimen through Nakazima punch stretching test and the experimental FLD.

Preprints (www.preprints.org) | NOT PEER-REVIEWED | Posted: 16 October 2018 doi:10.20944/preprints201810.0353.v1

(a)

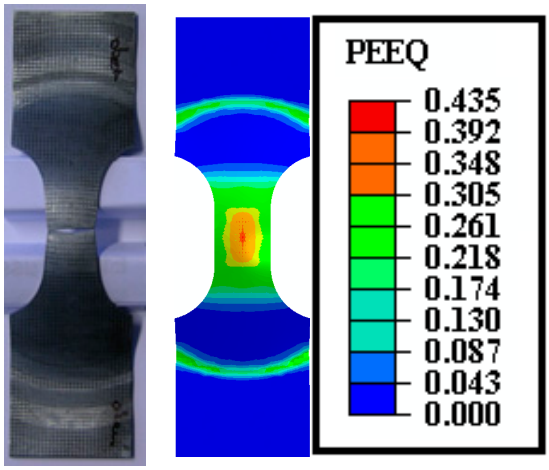

(b)

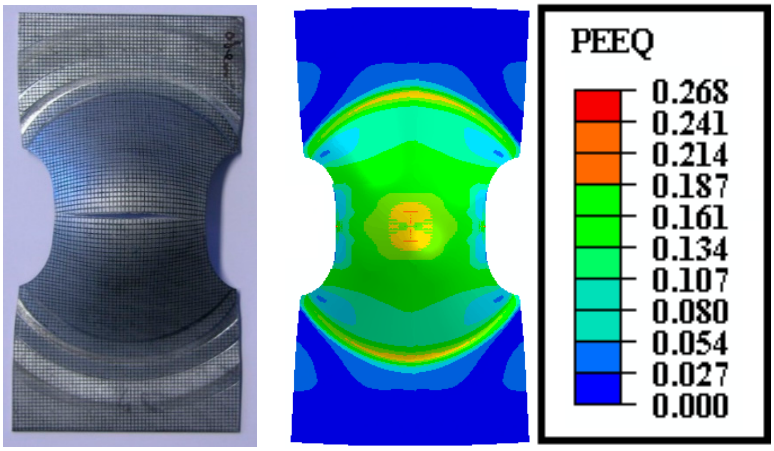

(c)

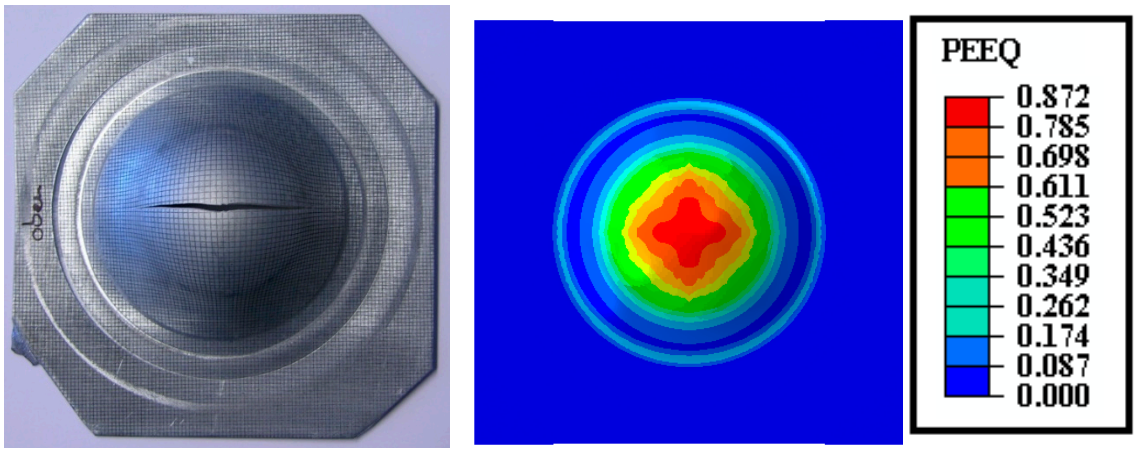

Fig. 7. The comparison of equivalent plastic strain distribution and fracture location for specimens with (a) 15, (b) 45, and (c) 115 mm width.

Preprints (www.preprints.org) | NOT PEER-REVIEWED | Posted: 16 October 2018 doi:10.20944/preprints201810.0353.v1

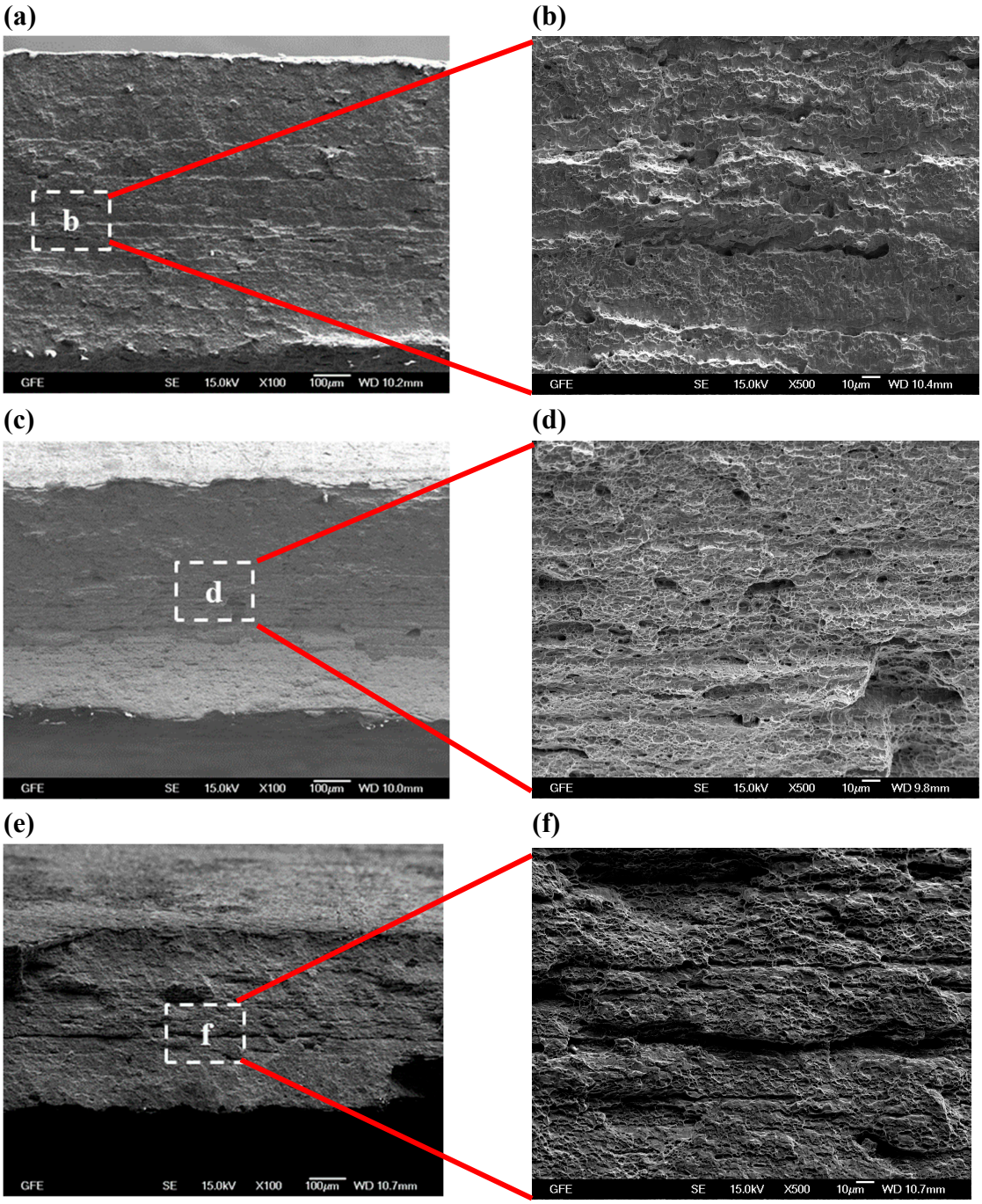

Fig. 8. The fracture surfaces of Nakazima test specimens with (a) and (b) 15, (c) and (d) 45, and (e) and (f) 115 mm width. This Figure is adopted from ref. [28].

Preprints (www.preprints.org) | NOT PEER-REVIEWED | Posted: 16 October 2018 doi:10.20944/preprints201810.0353.v1

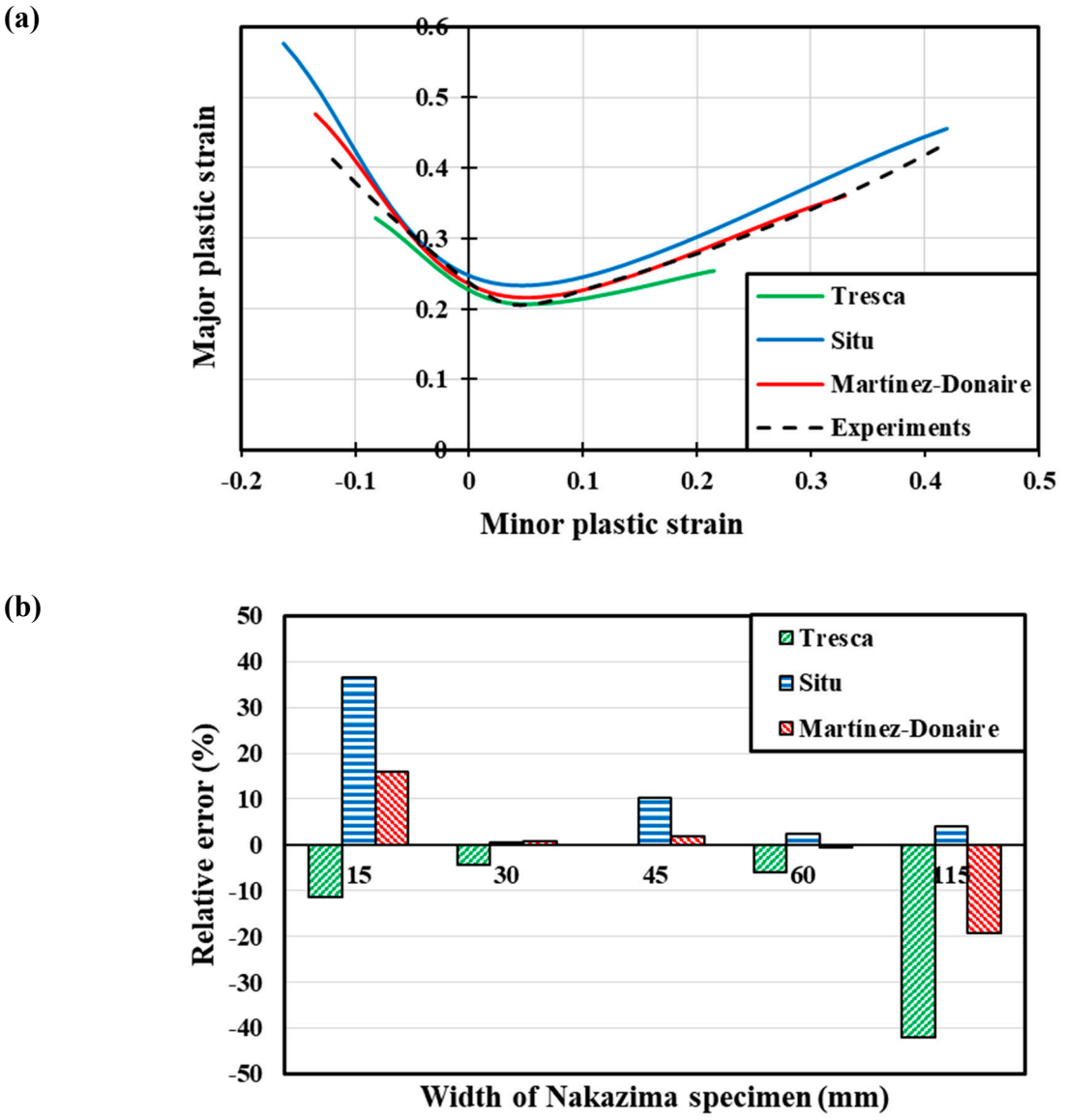

Fig. 9. The comparison between simulations and experiments of Nakazima tests; (a) the predicted FLDs, and (b) the relative errors of equivalent plastic strain for each specimen geometry and model.

Preprints (www.preprints.org) | NOT PEER-REVIEWED | Posted: 16 October 2018 doi:10.20944/preprints201810.0353.v1

(a)

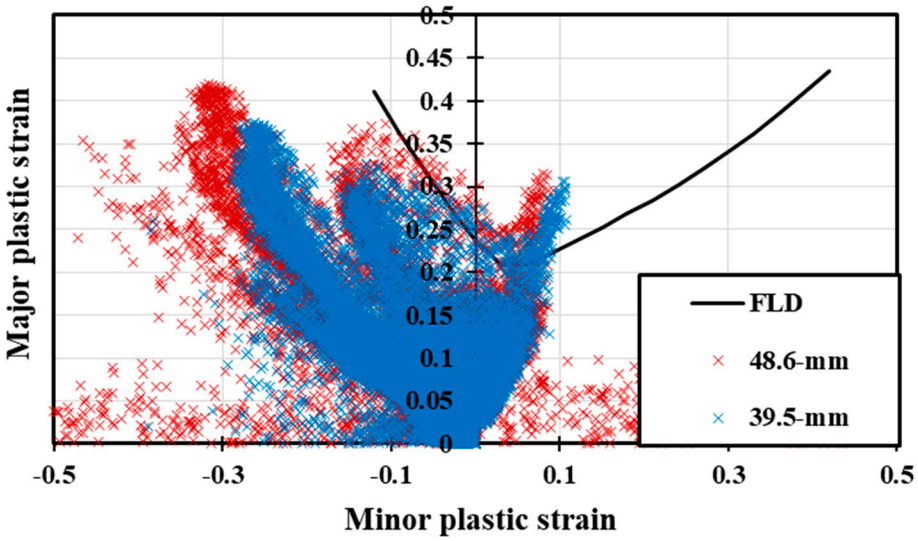

(b)

Fig. 10. Experimental results of cross-die tests, (a) strain distribution, and (b) the final product with height of 48.6 mm.

Preprints (www.preprints.org) | NOT PEER-REVIEWED | Posted: 16 October 2018 doi:10.20944/preprints201810.0353.v1

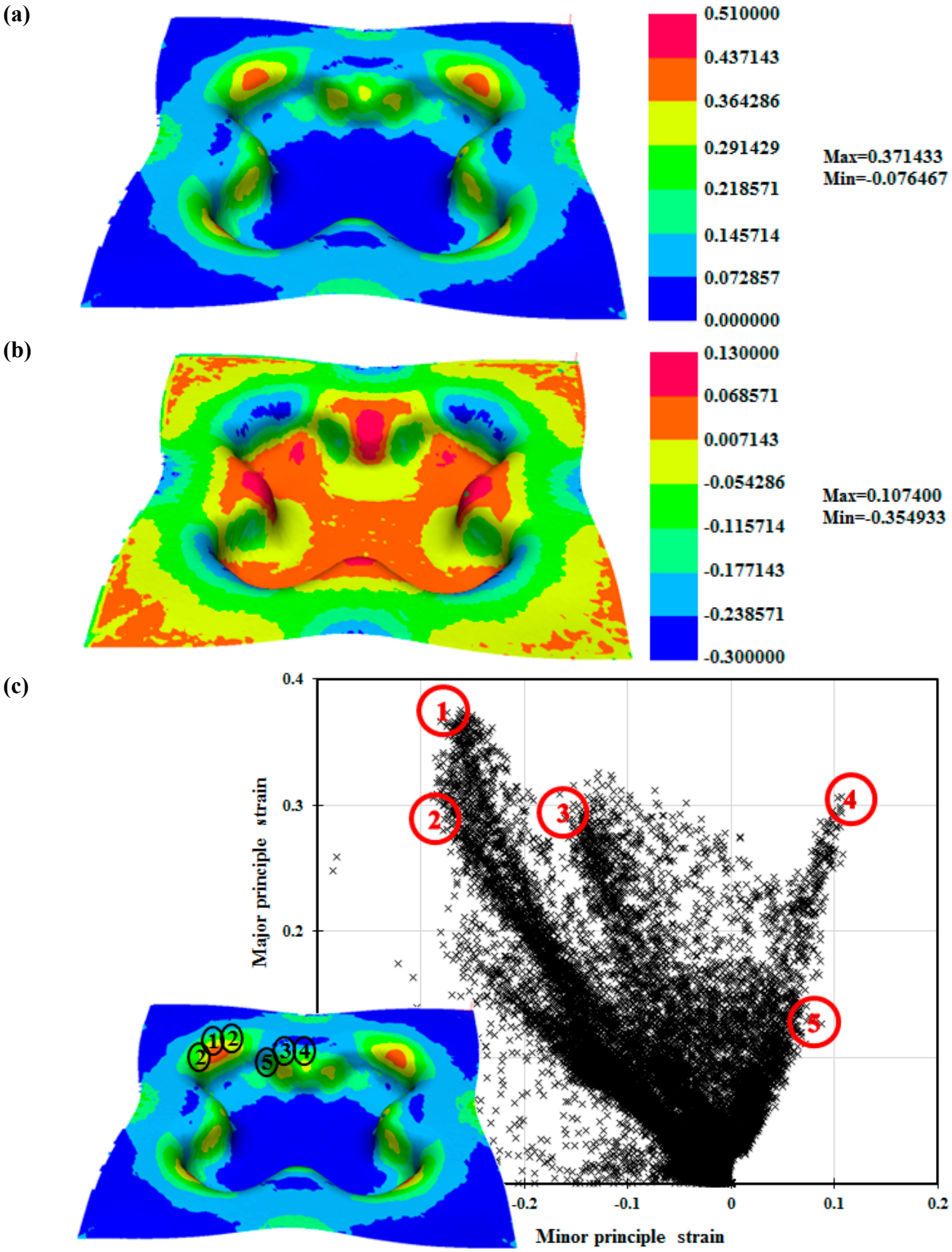

Fig. 11. The experimental data of final product with 48.6 mm height which was measured using PHAST^{TM} equipment; (a) Major strain distribution, (b) minor strain distribution, and (c) measured strains for the different locations.

Preprints (www.preprints.org) | NOT PEER-REVIEWED | Posted: 16 October 2018 doi:10.20944/preprints201810.0353.v1

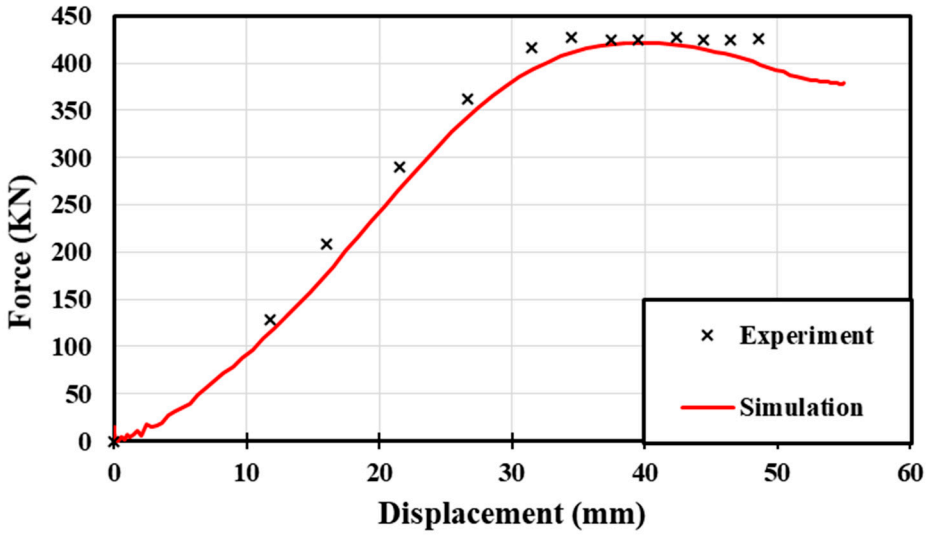

Fig. 12. Force-displacement responses through experiment and simulation of cross-die test.

Preprints (www.preprints.org) | NOT PEER-REVIEWED | Posted: 16 October 2018 doi:10.20944/preprints201810.0353.v1

(a)

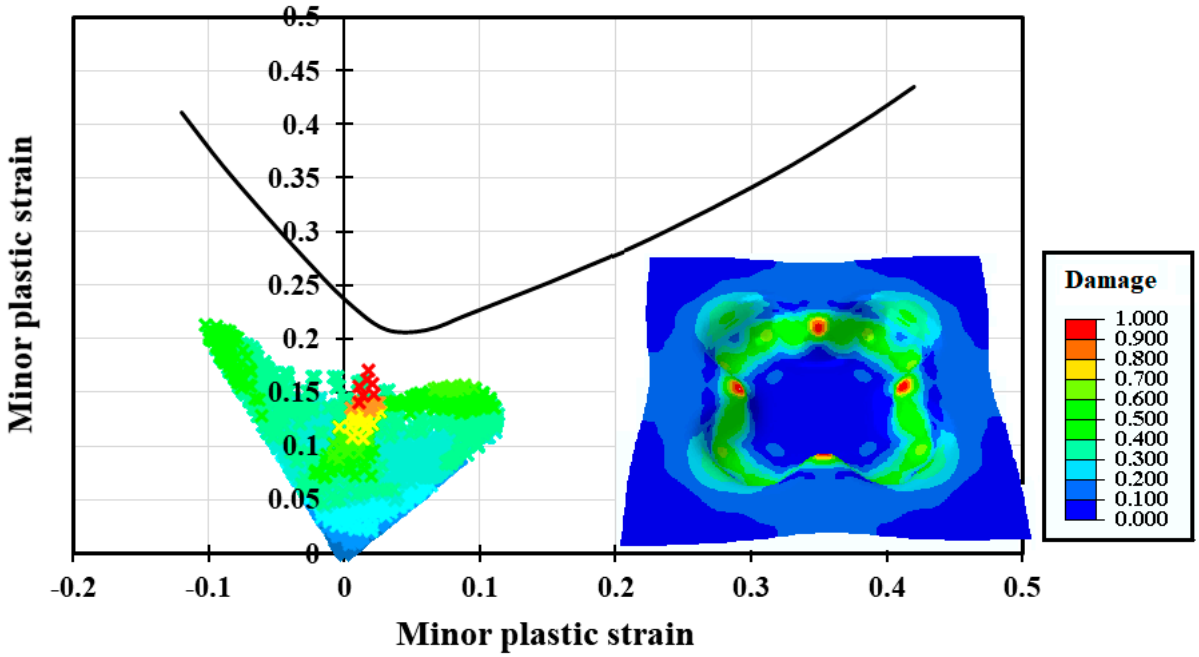

(b)

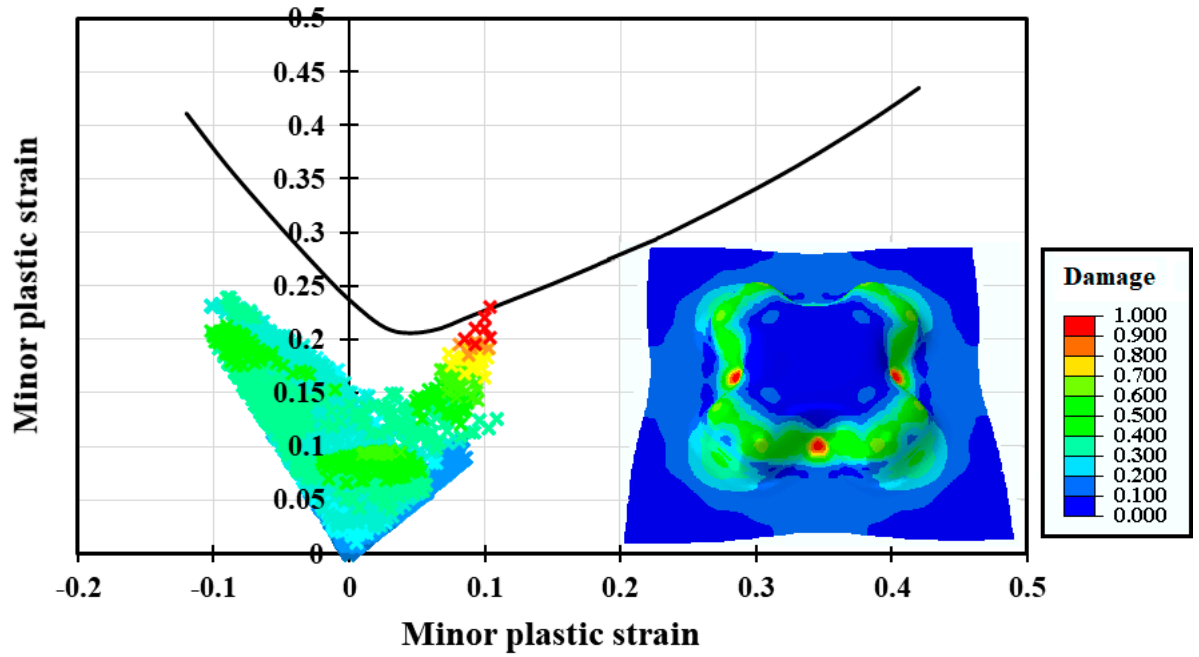

Fig. 13. Global strain status and the damage indicator at the integration points located at (a) the negative surface, and (b) the positive surface (the colors represent the values of damage indicator calibrated by experimental FLD).

Preprints (www.preprints.org) | NOT PEER-REVIEWED | Posted: 16 October 2018 doi:10.20944/preprints201810.0353.v1

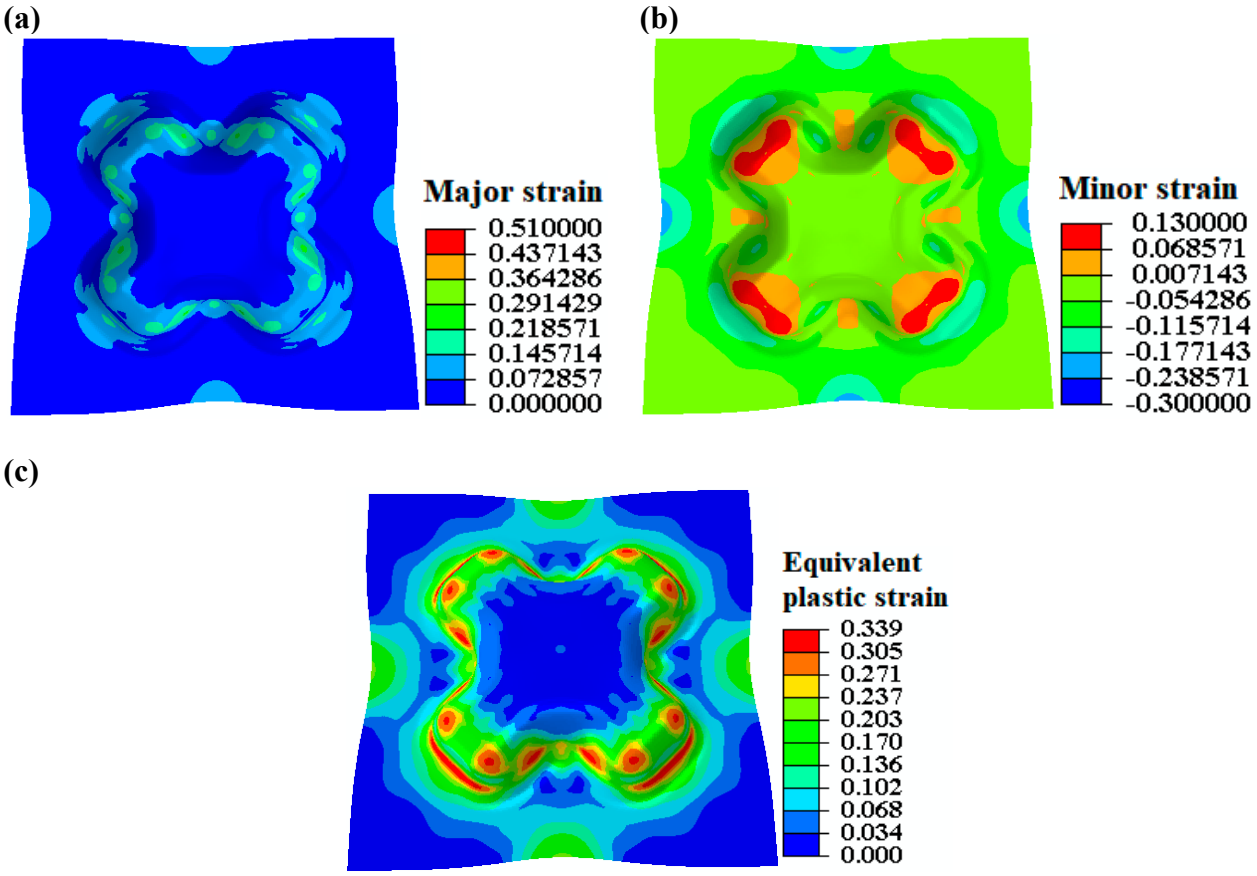

Fig. 14. The simulation results for cross-die deep drawing test. Distribution of major, minor, and equivalent plastic strains at the onset of damage represented in (a), (b), and (c), respectively; (the experimental FLD was assumed as the damage criterion).

Preprints (www.preprints.org) | NOT PEER-REVIEWED | Posted: 16 October 2018 doi:10.20944/preprints201810.0353.v1

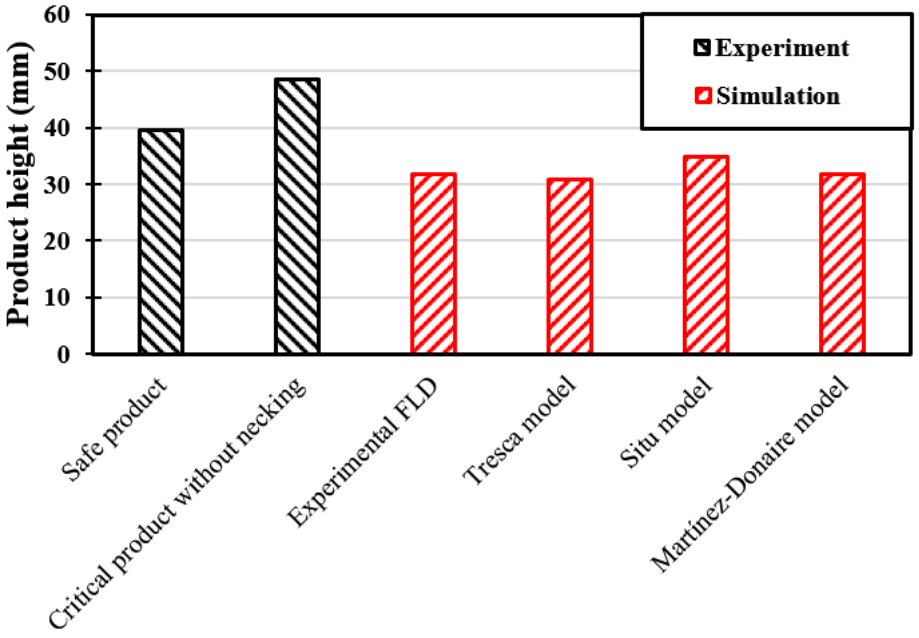

Fig. 15. The calculated height of the final products.